

Article

Soft Coiled Pneumatic Actuator with Integrated Length-Sensing Function for Feedback Control

Jacob R. Greenwood [†]  and Wyatt Felt ^{*,†} 

VPI Technology, Draper, UT 84020, USA

* Correspondence: wyattf@vpitech.com

† These authors contributed equally to this work.

Abstract: SPIRA Coil actuators are formed from thin sheets of PET plastic laminated into a coil shape that unfurls like a “party horn” when inflated, while many soft actuators require large pressures to create only modest strains, SPIRA Coils can easily be designed and fabricated to extend over dramatic distances with relatively low working pressures. Internal metalized PET strips separate in the extended portion of the actuator, creating an electrical circuit with a resistance that corresponds to the actuator length. This paper presents and experimentally validates easy-to-use design models for the actuators’ self-retracting spring stiffness, its pneumatic extension force, and its internal length-sensing electrical resistance. Testing of the self-sensing capabilities demonstrates that the embedded sensor can be used to determine the actuator length with virtually no hysteresis. Feedback control with the resistance-based sensing resulted in length-control errors within 5% of the extended actuator length (i.e., 3 cm of 60 cm).

Keywords: soft robotics; pneumatic actuators; resistance sensing



Citation: Greenwood, J.R.; Felt, W. Soft Coiled Pneumatic Actuator with Integrated Length-Sensing Function for Feedback Control. *Actuators* **2023**, *12*, 455. <https://doi.org/10.3390/act12120455>

Academic Editor: Hamed Rahimi Nohooji

Received: 28 October 2023
Revised: 27 November 2023
Accepted: 4 December 2023
Published: 8 December 2023



Copyright: © 2023 by the authors. Licensee MDPI, Basel, Switzerland. This article is an open access article distributed under the terms and conditions of the Creative Commons Attribution (CC BY) license (<https://creativecommons.org/licenses/by/4.0/>).

1. Introduction

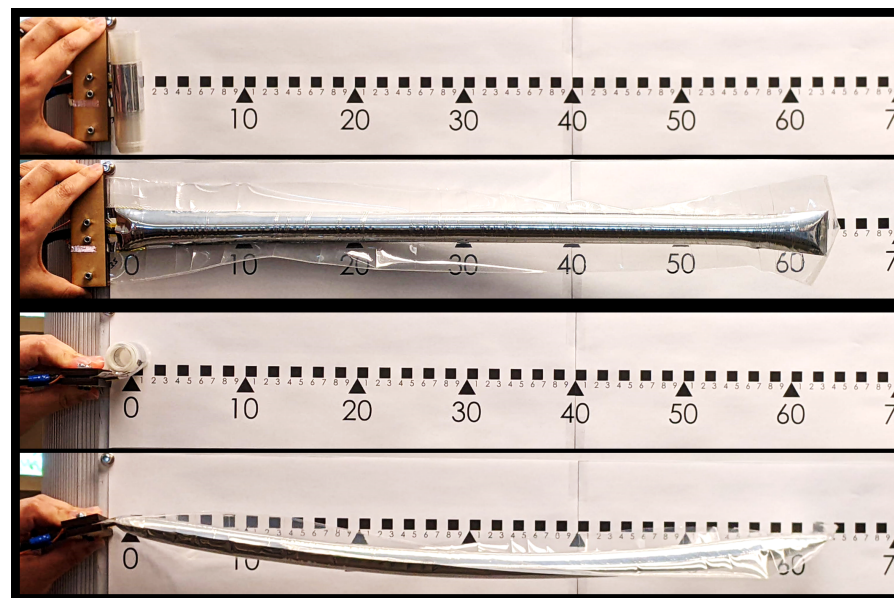
The development and application of a wide-variety of soft pneumatic actuation techniques has led to extensive innovation in mechanisms and robotics [1–3]. Typically made from elastomers, fabrics, or thin plastics, these soft actuators are driven by the expansion of an internally contained volume of air. The actuators tend to behave in a “soft” or compliant way because the materials are often flexible and the air is compressible. Examples of common soft pneumatic actuators include axially contracting fiber-reinforced actuators, bellows-like axially extending actuators, and bellows-like bending actuators (which reinforce one side of the actuator to convert the extension into bending).

While these actuators have shown great versatility in their applications, the distance over which these actuators can traverse is fundamentally limited to some fraction or multiple of their initial length. Contracting fiber-reinforced actuators and “peano” actuators, for example, can typically only reduce their length by less than 50% [4,5]. Bellows-like actuators, on the other hand, can extend in an accordion-like manner to several multiples of their contracted length when pressurized. Correspondingly, when subjected to vacuum pressure, bellows-like structures can act as contractile actuators with dramatic contraction ratios [6–8]. The ratio of the extended length to the contracted length is limited, however, by the thickness of the many folds.

In many ways, the extended length of soft pneumatic actuators is limited by the ability to efficiently store the material needed to enclose the air volume as it expands. Some actuators achieve their motion by stretching elastomeric bladders. However, these often require substantial amounts of pressure to stretch the elastomers. Furthermore, there are limits to the strain these materials can undergo. Larger strains can often be accomplished by using membrane-reinforced actuators that use bending or unfolding pleated structures [4,5,7]. Recently, there has been exploration of pneumatically actuated

structures that extend by inverting [9,10] or un-spooling thin tubes [11]. These long thin tubes allow the actuators to extend over dramatically long distances.

This paper introduces a novel, self-sensing coiled actuator called a “SPIRA Coil”, which stands for Soft Self-Sensing Pneumatic Integrated Retractable Actuator Coil. A SPIRA Coil is formed from thin sheets of plastic that are laminated into a coil shape. When air is added to the interior volume of the actuator, it extends like a party horn (Figure 1b). When air is removed, it retracts towards its coiled shape. Because the materials are so thin when deflated, the actuator can extend and retract over dramatic distances compared to its initial size. In this work, actuators with a coiled outer diameter of approximately 2 cm were able to extend 60 cm.



(a)



(b)

Figure 1. The SPIRA Coil actuator presented in this work, (a) shown both retracted and extended, is similar in mechanism to a “party horn” (b) and can extend to dramatically long lengths from a tightly wound coil. Unlike a party horn, SPIRA Coils can sense their own extension through the resistance of an internal circuit, allowing the length of the actuator to be measured and controlled for robotic applications. The ruler shown in (a) is in cm.

Like other soft actuators, the party-horn-like actuator presented in this work could not easily be combined with traditional mechanical sensors without compromising its unique features [12]. Accordingly, SPIRA Coils are designed with sensing integrated into their structure. The interior volume is formed from two layers of PET with a thin metalized layer. The air in the expanded section of the actuator separates these two layers. At the point where the coil begins, the two layers are pressed together, forming an electrical circuit between the air-inlet end of the actuator and the beginning of the coil (Figure 2). As the actuator extends, the length of the circuit increases, making the resistance proportional to the actuator length.

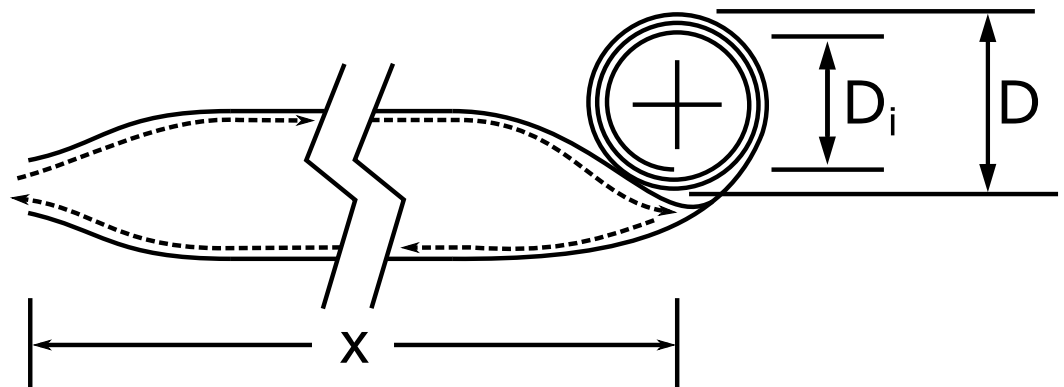


Figure 2. A cross-section of a partially deployed actuator. The conductive path for resistance sensing is shown as a dashed line. Shown also is the corresponding length of the actuator x , the diameter D , and inner diameter D_i .

This paper introduces the SPIRA Coil actuator, describes how it can be readily fabricated with inexpensive materials, and presents and validates easy-to-use design models for the actuator's self-retracting spring stiffness, its pneumatic extension force, and its internal length-sensing electrical resistance. This paper also presents the use of the resistance-based length sensing in the feedback control of the actuators.

2. Background

2.1. Party Horns and Coiled Inflatable Booms

The coiled spiral pneumatic mechanism presented in this work is very similar to that of the “party horn” (Figure 1b). Though the name in English is somewhat ambiguous, other languages have more unique monikers (German—*rollpfeife*, *luftriessel*; Spanish—*espantasuegras*; Italian—*lingua di Menelik*; Japanese—*fukimodoshi*) some of which date back more than a century to the popularity of the horn in carnival celebrations. Despite the ubiquity of the mechanism in popular culture, with little exception [13], it has been largely ignored by the robotics community.

In contrast, non-retracting coiled inflatable booms have been the subject of extensive research. These are pneumatic tubes that have been flattened, wrapped around a hub, and designed to unroll as they are inflated [14]. A coiled boom may be advantageous due to its simplicity [15] and the potential for high packing efficiency [16]. Typically inflatable booms, both coiled and uncoiled, use metal-polymer laminates as their membrane [14,15,17–19].

There are, however, known issues with coiled inflatable booms. The thickness of the material, for example, often causes issues (ex. wrinkling, local buckling) during the coiling process [14,17,19,20], while alternate wrapping methods have been suggested that accommodate thickness [21–23]; these methods do not include a sealed inner volume and thus are not suitable for pneumatic actuator use.

The SPIRA Coil fabrication method introduced in this paper solves many of these issues. Rather than rolling up a flat tube, which could introduce wrinkles and local buckling, the layers of the SPIRA Coil prototypes are adhered only after they have been coiled, allowing the layers to shift relative to one another prior to adhesion. The compromise of this method is the slight curvature introduced into the inflated actuator.

Another issue of non-retracting inflatable booms is the potential that they can uncoil in an unpredictable manner. The dynamics and geometry of inflatable booms during deployment have been studied and simulated by [24–28]. Results have found that the deploying motion can be unstable, unpredictable, chaotic, and even catastrophic [15,20,27], particularly in an orbital environment. Researchers have tried to address this by using hook-and-loop strips [29], adhesive [26], and flexible plates [30] as methods to slow down deployment.

In contrast, just like a party horn, the self-retracting SPIRA coil extends and retracts in a predictable way. This is partly encouraged by changes in the relaxed coil diameter along the length of the actuator—an unavoidable result of the fabrication process. This changing diameter, combined with the restricted airflow to the coiled section, creates conditions that encourage the actuator to unfurl sequentially and predictably.

2.2. Plastic Annealing of PET

Polyethylene terephthalate (PET) is a common material used in deployable booms and other origami applications [14,31,32]. It has been demonstrated that heating a sheet of PET can relieve internal stresses without causing softening of the material [33]. This plastic annealing effectively resets the natural state of the PET so that, when the sheet is cooled, the PET remains in the as-heated shape.

This method was analyzed for use in origami applications [34] and has been demonstrated in a medical support system to mitigate buckling [35], lamina emergent origami [36], and in developable mechanisms [37]. This simple plastic annealing process can be very useful as it can change the energy behavior of the material, allowing the user to select different stable and unstable states [38].

2.3. Constant Force Springs

The self-retraction of the SPIRA Coil actuator is enabled by a material structure that closely resembles that of a “constant force spring”. Votta’s equation for the retraction force, F_R , of a constant force spring of natural diameter D_n is

$$F_R = \frac{Ebt^3}{26.4\left(\frac{D_n}{2}\right)^2} \quad (1)$$

where E is the Young’s modulus of the material, b is the spring’s width, and t is the spring’s thickness [39].

3. Design

The actuator is made using readily-available materials. The walls of the actuator’s inflatable chamber are made of metalized PET. These sheets also provide the conductive path for the integrated resistance sensing. The exterior of the actuator is made from PET laminate material (heat-activated adhesive backed with PET), which bonds the actuator together and provides the pneumatic seal. A lay-flat PET tube is inserted at the open end of the actuator to allow air to enter once sealed, and shims are placed on the sides to help the edges properly adhere.

All of these layers are then rolled up on a mandrel. During the rolling process the layers are allowed to shift end-to-end, which prevents the wrinkling and local buckling often observed in coiled booms (see Section 2.1). Once rolled up and secured, the layers are then heat-treated. The heat treatment melts the heat-activated adhesive which bonds and seals the actuator together. The heat also serves to plastically anneal the PET material, relaxing the internal stresses. Once cooled, the actuator remains in the coiled shape.

After heat treatment, the shims and mandrel are removed and the formed actuator acts as a coiled PET spring with an integrated pneumatic chamber. As air enters the pneumatic chamber, the spring force is overcome, and the actuator unrolls and provides structure. As air is removed, the spring force rolls the actuator back up. In other words, the extension force comes from the air pressure, while the retraction force comes from its spring-like behavior.

The conductive aluminum of the metalized PET forms the circuit used in resistance sensing, as shown in Figure 2. During the extension and retraction, the metalized PET separates in the inflated portion and connects again at the coil (where the aluminum on one side of the chamber contacts the aluminum on the other side of the chamber). Hence, the resistance of the separated aluminum corresponds to the inflated length of the actuator.

3.1. Construction

The construction of each actuator is shown in Figure 3 and described below. A video of how to fabricate a SPIRA Coil actuator can be found in the Supplementary Materials as Video S2 (the video has minor changes to the steps below).

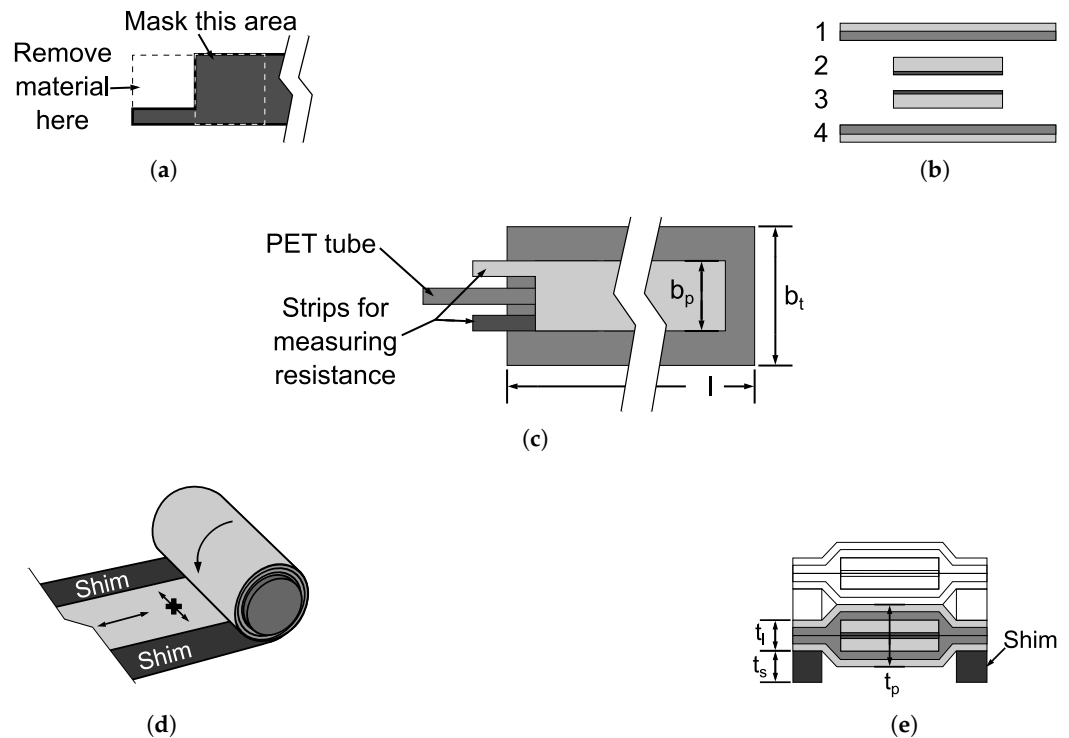


Figure 3. Steps in the manufacture of an actuator: (a) cut and mask the metalized PET (b,c) layer as shown; (c) insert PET tube (top laminate layer not shown); (d) place shim material, roll up, secure, and heat-treat in oven. Subfigure (e) shows a cross-section of two layers of a rolled-up actuator after heat treatment (not to scale).

First, two metalized PET layers are cut to width b_p and length l . These layers should be cut and masked as shown in Figure 3a, which allows the conductive layer to be accessible outside of the actuator without allowing the pressurized air to escape. The masking (placed on the conductive side of the material) prevents contact between the aluminum layers at the base of the actuator, as this area may become partially pinched during actuation.

Second, two strips of PET laminate are cut to width b_t and length l and the four strips are stacked together as follows (see Figure 3b):

1. PET laminate (adhesive face down);
2. Metalized PET (aluminum face down);
3. Metalized PET (aluminum face up);
4. PET laminate (adhesive face up).

Layers 2 and 3 should be shifted such that the strips for measuring resistance extend beyond the PET laminate as shown in Figure 3c. A laid-flat PET tube is inserted between layers 2 and 3, which will allow air to enter the sealed chamber in the completed actuator. A few centimeters of the opposite end can be adhered to prevent those ends from sliding during the rolling process.

Due of the difference in thicknesses between the laminate-only and pneumatic sections of the final actuator, a flexible shim must be chosen such that $t_p \approx t_l + t_s$. These disposable shims are placed over the laminate-only layers (see Figure 3e) during the fabrication process. This ensures that an adequate adhesive bond is made throughout the actuator.

Next, the layers are rolled up on a mandrel of diameter D_i , as shown in Figure 3d. Care should be taken that the layers do not shift side-to-side during the rolling process and to ensure that the electrical circuit is not compromised. Excess laminate material will accumulate at the unrolled end and can be trimmed. Secure the completed roll and place in an oven at approximately 160 °C until all the adhesive has bonded. The shims should be removed after the actuator has cooled.

For this paper, we used the materials found in Table 1.

Table 1. Materials used in this paper.

Material	Thick.	Vendor	Part No.
Metalized PET	2 mil	McMaster-Carr	7538T11
PET Laminate	5 mil	USI-Laminate	1146
Masking Polyimide	1.5 mil	McMaster-Carr	1754N13
PET Shim	5 mil	Various	Various

4. Model

The presented actuator can be modeled as a constant force spring and as a pneumatic cylinder. Hence, the force model can be viewed in two interlocking pieces: the spring model (for retraction), and the pneumatic model (for extension). Resistance sensing is also modeled.

4.1. Retraction: Spring Model

The spring model is based on Equation (1), with adjustments for different sections of our actuator. The actuator can be modeled as a constant force spring with two sections—pneumatic and laminate-only. The spring forces for these sections add in parallel and have the same diameter. The modulus of elasticity E , width b , and thickness t vary between these sections and will be noted by subscripts p and l for pneumatic and laminate-only, respectively, as shown in Figure 3.

If we assume that the diameter of the actuator is constant along its length ($D = D_i$), then the retraction force of the actuator, F_R , is

$$F_R \approx \frac{E_l(b_l - b_p)t_l^3 + 2(E_p b_p (\frac{t_p}{2})^3)}{26.4(\frac{D_i}{2})^2} \quad (2)$$

which considers the force from the pneumatic section to be the force of two identical springs of thickness $\frac{t_p}{2}$ in parallel.

For actuators in a coiled natural shape, the diameter, D , changes along the length x of the coil due to the thickness of the material. One way to approximate the diameter of a wrapped coil of a given length l is to calculate the cross-sectional area of the coil [40]. Since the cross-sectional area remains the same between coiled and uncoiled:

$$lt_p = \pi(\frac{D_o}{2})^2 - \pi(\frac{D_i}{2})^2 \quad (3)$$

where l and t_p are the length and thickness of the coiled sheet, and D_o and D_i are the outer and inner diameters of the coil. Solving for the outer diameter, D_o , we obtain

$$D_o = 2\sqrt{\frac{lt_p}{\pi} + (\frac{D_i}{2})^2} \quad (4)$$

We can also solve for the coil diameter D at intermediate states, where some length of material x is uncoiled and the rest of the material, $l - x$, is coiled:

$$D = 2\sqrt{\frac{(l-x)t_p}{\pi} + (\frac{D_i}{2})^2} \quad (5)$$

Combining Equations (2) and (5), we obtain an equation for the retraction force of our actuator, F_R , as a function of the deployed length:

$$F_R = \frac{E_l(b_t - b_p)t_l^3 + 2(E_p b_p (\frac{t_p}{2})^3)}{26.4(\frac{t_p(l-x)}{\pi} + (\frac{D_i}{2})^2)} \quad (6)$$

4.2. Extension: Pneumatic Model

Neglecting losses and elastic energy storage, the pneumatic extension force F_E is the product of the internal gauge pressure P and the change in volume per unit length $\frac{dV}{dx}$

$$F_E = P \frac{dV}{dx}. \quad (7)$$

The change in volume per unit length $\frac{dV}{dx}$ is equal to the cross-sectional area of the inflated portion of the actuator A_{pneu}

$$F_E = P A_{pneu}. \quad (8)$$

Except for the portion near each end, we assume that the pressure will force the cross-section the inflated portion to be circular, thus maximizing the volume within the constrained perimeter length. If we assume the cross-section is circular, then we can replace A_{pneu} with an expression based on circumference of the circle being equal to twice the width of the inflatable section, b_p

$$F_E = P \frac{b_p^2}{\pi}. \quad (9)$$

Because our actuator has a constant cross-section, this result matches with those obtained by [27,28].

4.3. Sensing: Resistance Model

The self-sensing of the actuator is performed by measuring the resistance of the vacuum-deposited aluminum that “metalizes” the inner PET layers. This resistance value can then be correlated with the length of the actuator.

The resistance of a wire can be found using the following equation:

$$R_{wire} = \frac{\rho_{wire} l_{wire}}{A_{wire}} \quad (10)$$

where ρ_{wire} is the resistivity, l_{wire} is the length, and A_{wire} is the cross-sectional area of the wire. For our application, the wire is the metalized PET strips. Assuming the vacuum-deposited aluminum has a constant thickness t_{al} , the resistance is a linear function of the length of the inflated portion of the actuator, x :

$$\Delta R = \frac{2\rho_{al}x}{b_p t_{al}} \quad (11)$$

In the case that the actuator completely extends, the metalized PET strips may completely separate and no electrical connection is made. This makes it easy to measure when the actuator is fully extended. The connection will be restored when the actuator starts to roll back up into an intermediate state.

5. Testing

5.1. Test Setup

The testing was primarily performed using a tensile test machine and custom fixture plates, as shown in Figure 4. The base of each actuator was clamped in the bottom fixture, which has a channel for the pneumatic inlet tube and copper contacts for electrical connection with the resistance sensor. The top fixture was constructed using a polished steel shaft which rolls in ultra-low-friction PTFE dry-running sleeve bearings and is covered

by 12.7 mm (1/2") PTFE tubing. This allows the length of the actuator to be controlled and measured with the rolling portion of the actuator free to roll and slide on the rod with minimal friction. The force data found by the tensile test machine (F_M) is the sum of the pneumatic force (F_E) and the spring force (F_R), which include frictional losses.

The tensile test machine fully extended and retracted the actuator several times while collecting corresponding force data. Meanwhile, a simple pneumatic system was controlling the air pressure inside the actuator. A video of one cycle of a test is included in the Supplementary Materials as Video S3.

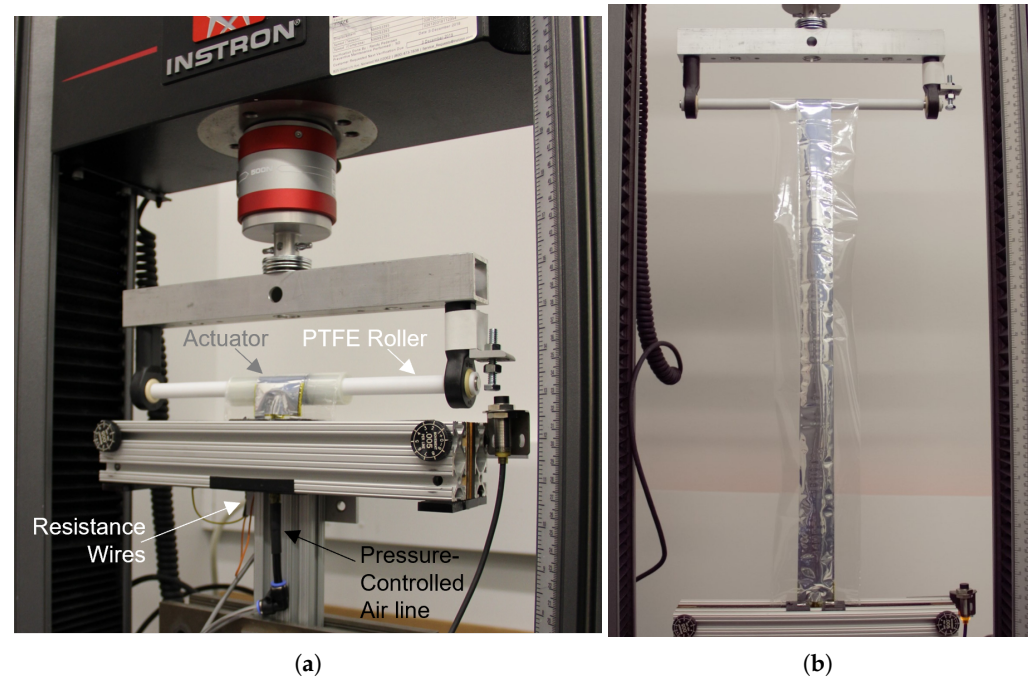


Figure 4. (a) A tensile test machine was used to test various actuators under tightly controlled internal pressure conditions. (b) The actuators were tested at lengths up to 60 cm from their relaxed length.

5.2. Material Characterization

The effective modulus of elasticity for each of two sections of the actuator in Equation (2) was characterized based on sample measurements performed on the tensile test machine. Coils of laminate–laminate and laminate–metalized PET were prepared and tested on using the same setup as described above. From this data we estimated the modulus of elasticity values as approximately $E_p = 5$ GPa and $E_l = 3$ GPa.

All the actuators shown were made using the same batch of metalized PET. We assume the aluminum has a constant thickness throughout the batch and that the aluminum has a resistivity of $\rho_{al} = 2.65 \times 10^{-8}$ Ohm \cdot m. The resistance of a 2-cm-wide, 60-cm-long sample strip of metalized PET was measured to be 37.07 Ohms. Using Equation (10), the approximate thickness of the aluminum was calculated as $t_{al} = 1.87 \times 10^{-8}$ m.

5.3. Spring Force Response

The spring response of the actuators was tested using the test setup described above with the tube inlet left open (Figure 5). The open tube ensured zero gauge pressure in the pneumatic section of the actuator ($F_E = 0$). Hence, the force measured by the tensile test machine is the spring force ($F_M = F_R$), which is considered to include hysteresis-inducing losses.

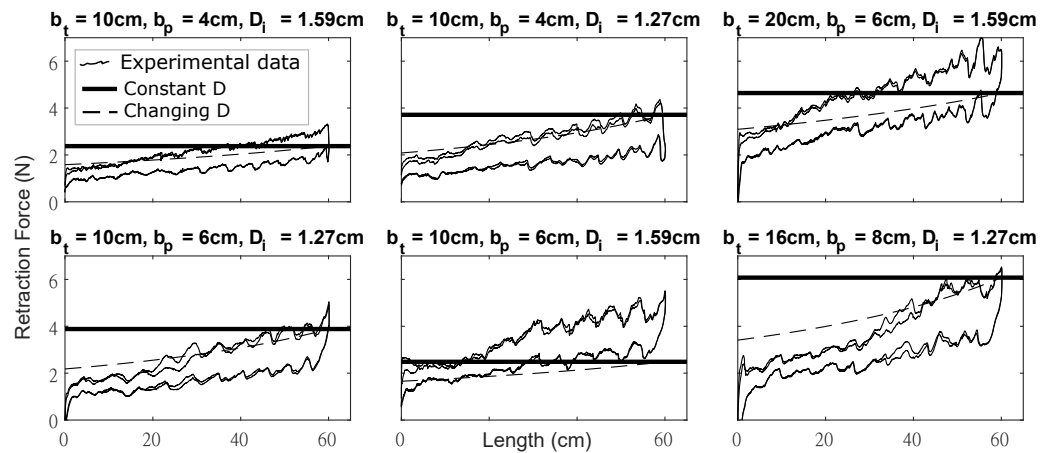


Figure 5. Measured spring retraction force compared to the model-predicted forces presented in Section 4.1 for six different actuators.

5.4. Pneumatic Force Response

The pneumatic force response testing was similar to the spring response testing but involved a constant applied pressure to the actuators' pneumatic input. A simple pressure controller with a large pneumatic accumulator was used to maintain constant pressure in the actuator during tensile testing. In order to keep the coil end of the actuator in consistent contact with the rolling shaft, the magnitude of the pressure was limited to those pressures which allowed the actuator to maintain tension on the test fixture in both extension and retraction. If a larger pressure was used, then fixture would apply compressive forces to the actuator, confounding the results and often causing the actuator to buckle and/or slip out of the fixture. This not only limited the number of distinct pressures that individual actuators could be tested at but limited the number of actuators that could be tested at multiple pressures.

5.5. Resistance Sensing

To achieve an accurate resistance measurement, a sufficient amount of pressure is needed to ensure that the metalized PET strips remain separated during actuation. In free extension and retraction, the actuator maintains sufficient back pressure for resistance sensing (for more details, see Section 6.3). It is also important to provide sufficient masking on the metalized PET, as described in Section 3.1.

The resistance was measured using a simple DAQ and voltage divider simultaneous with the pressure-response tests described earlier.

6. Results and Discussion

6.1. Spring Force Response

As can be seen in Figure 5, the model-predicted force values overlapped with the experimentally measured values. In almost every case, using the more complex, changing-diameter model (Equation (6), dashed line) resulted in a more accurate spring-force prediction than the simpler, constant-diameter model (Equation (2), thick solid line). The model, however, does not account for the evident hysteresis in the response.

6.2. Pneumatic Force Response

The results, shown in Figure 6, show the pneumatic force of several actuators ($F_E = F_M - F_R$) compared to the model predictions. The plotted experimental values have the spring component of the force (from Figure 5) subtracted from them to isolate the net effect of the pneumatic pressure. The thick, dashed lines show the extension force predicted by the simple pneumatic model, Equation (9).

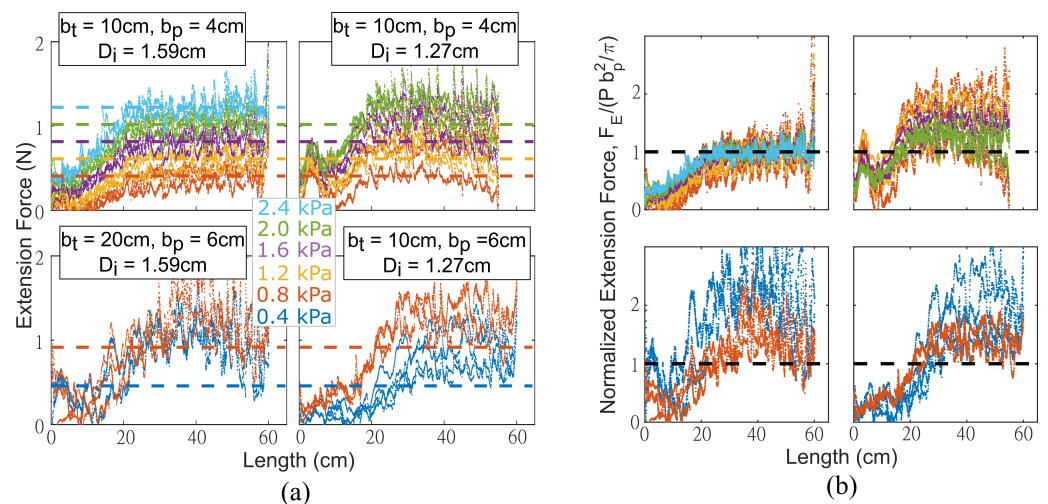


Figure 6. Extension force compared to the model prediction of Equation (9) for four different actuators. (a) The extension force plotted in these axes is defined as the measured tensile force minus the zero-pressure spring-retraction force for the same actuator. (b) These axes show the forces from (a) normalized by the model-predicted value (dashed lines).

At short extension lengths, the pneumatic force of the actuators starts small but, once a certain length is reached, the force becomes roughly constant, consistent with the constant force predicted by the model.

We again note that, to maintain tension in the fixture, the pressures shown in Figure 6 are lower than the self-extension of the actuators in unloaded conditions. The larger group of actuators shown in Figure 5 were found to have self-extension pressures that varied between 4 kPa and 9 kPa (0.6 psig to 1.3 psig).

Understanding the pneumatic force response of the actuator is an important step in the actuator design (e.g., to ensure equipment has sufficient pressures to actuate the device). In practice, once the minimum self-actuation pressure is met, the actuator extension is controlled more by mass than pressure. In the absence of external loads, the pressure inside the pneumatic chamber will equalize to the corresponding spring retraction force. Higher pressures do not always lead to higher extension forces. If the extension is constrained, the actuator may buckle or fold as internal pressure is increased. Hence, while the retraction force is controllable up to the maximum of the spring retraction force, the extension force is limited.

6.3. Resistance Sensing

Only one actuator prototype was free of manufacturing flaws and had sufficient retraction force to allow the resistance response to be reliably characterized on the tensile testing machine. As discussed previously, the pressure values at which we could test each actuator were limited. Some of these pressures were not large enough to fully separate the metalized PET layers along the entire length of the deployed actuator, creating an unusable resistance response at those pressures.

While this might seem like a problem, such low-pressure conditions are unlikely to be experienced by the actuator without active mass removal (i.e., vacuum). Pressurized self-extension produces sufficient back pressure for accurate resistance sensing. The same is true for self-retraction, where the back pressure is created by the flow restriction at the inlet. The experiments reported here included pressures that were lower than the pressures the interior volume would experience in most applications.

Further, several actuators had manufacturing flaws that affected the metalized PET. These flaws included the following: insufficient masking, inadvertent scoring and removal of aluminum along width of actuator, and buckling along wrinkle in laminate, allowing the PET strips to remain in contact in that area.

The resulting length to resistance data are shown in Figure 7. At extremely low pressures (i.e., below approximately 1.4 kPa or 0.2 psig), the resistance value was inconsistent due to insufficient back pressure, as discussed above. Above these pressures, however, the resistance response was very consistent and followed a similar trend to the linear response predicted by Equation (11) (black dashed line).

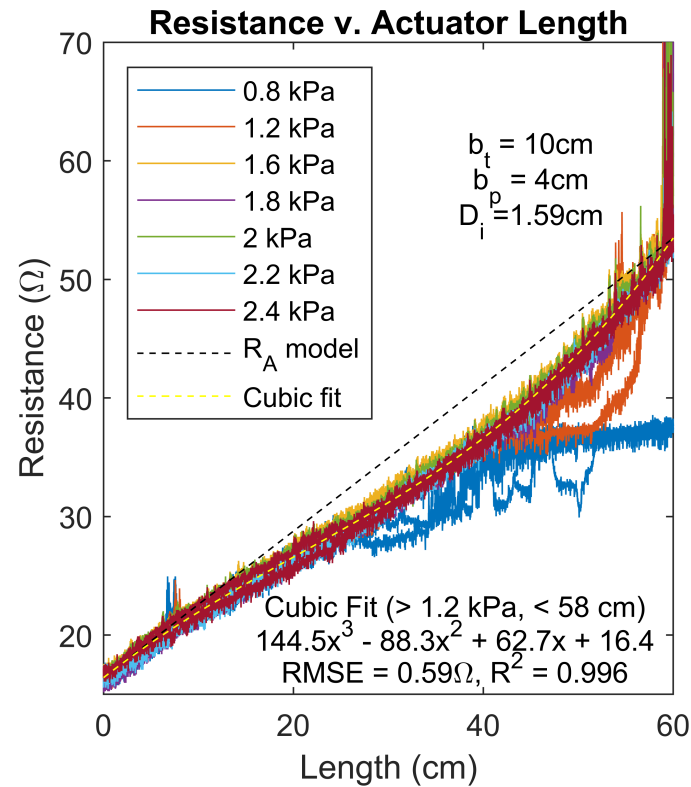


Figure 7. When a SPIRA Coil has sufficient pneumatic back pressure (in this case, ≈ 1.4 kPa or 0.2 psig), whether extending or retracting, the measured resistance can be used to determine the actuator length.

At full-extension, the calculated resistance became very high as the two sheets of metalized PET lost contact completely (nearly vertical lines in the top right of axes in Figure 7). This feature makes it very easy to identify the full-extension state of the actuator.

The measured resistance response at the pressures higher than 1.2 kPa and lengths less than 58 cm were fit with a cubic polynomial (yellow dashed line). The consistent response, virtually free from observable hysteresis allowed the cubic fit to describe nearly all the variance in the data, with an R^2 value of 0.996 and a corresponding RMSE of only 0.59 Ohms. This suggests that the measured resistance can reliably be used to calculate the length of the actuator for logging and control. Since the metalized layers are inside the sealed internal volume, they are protected from outside dust and debris.

7. Feedback Control

The predictable resistance response suggests that the measured resistance can reliably be used to calculate the length of the actuator for logging and control. This section demonstrates feedback control of SPIRA actuators using the integrated resistance sensing.

7.1. Feedback Test Setup

A vertical test fixture was created to test the use of the resistance in the feedback control of the actuators' length (Figure 8). The actuators were each connected to two small wooden mounting plates with thin layers of foam and strips of copper tape sandwiched between the plates and the actuator. The foam and copper ensured a consistent and reliable

connection to the metalized PET at the ends of the actuator. The actuator was clamped between these mounting plates and wires were attached to the copper tape as shown in Figure 8.

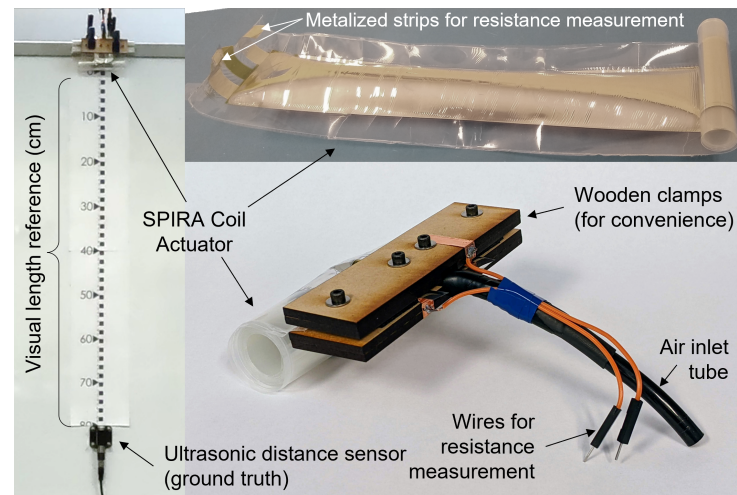


Figure 8. The SPIRA Coil actuator prototypes tested in Section 7.1 were outfitted with wooden clamps (for convenience), wires for resistance measurement, and an air inlet tube. Each actuator was connected to a vertical fixture for feedback testing using their internal-resistance-based length sensing. The vertical fixture included a printed ruler for visual length reference and an ultrasonic distance sensor for ground truth.

Next, the actuators were connected to a simple pneumatic system for adding and removing air, as well as an electronics system for measuring the actuators' resistance response. The actuator length in the fixture was measured by an ultrasonic distance sensor (DFRobot URM14, 1 mm accuracy).

A best-fit curve (second-order polynomial) relating the measured resistance to the actuator length (as measured by the ultrasonic sensor) was found for each actuator prior to feedback testing. The polynomial was used by the feedback controller to convert measured resistance values into estimated actuator lengths.

The actuators were then controlled using a simple proportional control algorithm, with the resistance providing the length estimate for feedback. Gain and dead-band values were chosen manually. The error in the commanded length was multiplied by a gain and used to drive the speed of a corresponding diaphragm pump. Two pumps and two solenoid valves were used, with one pair for inflation and the other for deflation. The nominal maximum flow rate of each pump was 12 L per minute (LPM) with a nominal power of 12 W.

The ultrasonic sensor was not included in the feedback loop and provided the ground truth for comparison. The sensor was specified to 1mm accuracy and $\pm 1\%$ error. However, due to its inherent limitations, the ultrasonic sensor was only able to capture distance data every 500 ms. The distance measurements happened during the first 100 ms of this window but were only reported by the sensor about 200 ms later. This may explain the slight time delay shown in the data. Spurious ultrasonic measurements were excluded from the reported data.

7.2. Feedback Results

The results from the feedback testing can be found in Figure 9, in a video included in the Supplementary Materials as Video S1, and in Table 2. As reported in Table 2, inspecting the measurement error between the feedback controller's resistance-based length estimate and the ultrasonic transducer measurement during the last five seconds of each commanded step, actuators 'a', 'b', and 'c' had steady-state respective length estimate errors of only 1%, 3%, and 2.3% on average, compared to the fully extended length of the actuators

(60 cm). For every commanded step across the three actuators, the average steady-state measurement error was less than 3 cm (5%).

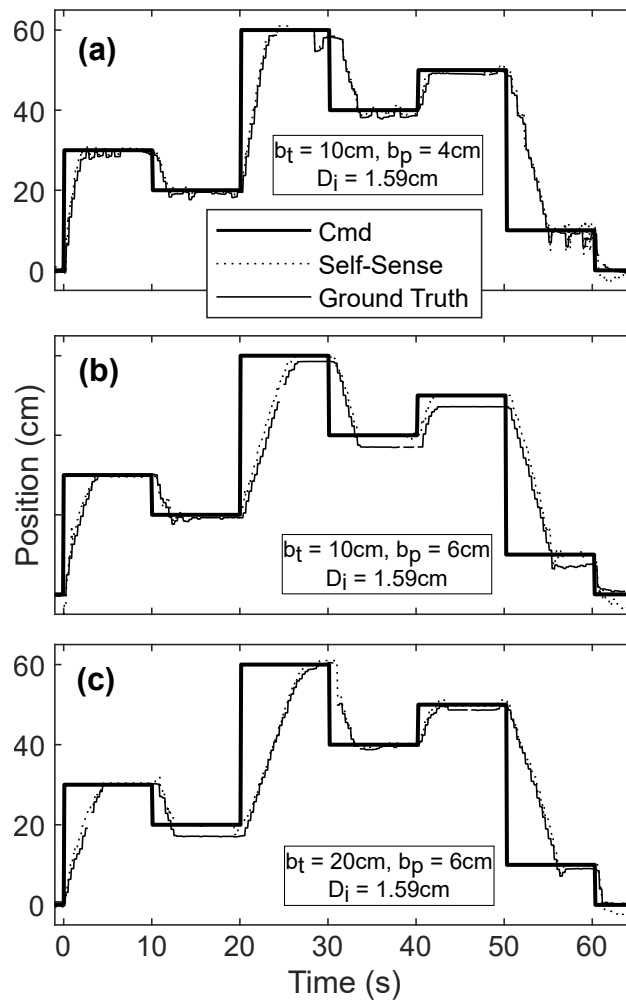


Figure 9. Time vs. distance graphs for three actuators (graphs ‘a’, ‘b’, and ‘c’ correspond to the three respective actuators) under feedback control. Internal metalized strips were used for the self-sense length feedback. Values from the ultrasonic sensor were used as the ground truth for comparison (and were not included in the feedback loop). Quantitative analysis is found in Table 2.

Table 2. A comparison of the measurement error (i.e., self-sensing value minus ground-truth) for the three actuators tested with feedback control during the last five seconds of each commanded step. Italicized values are in centimeters. The calculated percentage is based on the fully extended length of the actuator, 60 cm. Actuators ‘a’, ‘b’, and ‘c’ correspond to the respective actuators in Figure 9.

Measurement Error at Each Commanded Step, cm							
Act.	30 cm	20 cm	60 cm	40 cm	50 cm	10 cm	Average
(a)	0.46 (0.76%)	0.67 (1.11%)	0.03 (0.05%)	0.97 (1.61%)	0.71 (1.18%)	0.79 (1.32%)	0.60 (1.01%)
(b)	−0.30 (−0.50%)	1.00 (1.67%)	1.71 (2.84%)	2.74 (4.57%)	2.86 (4.77%)	2.82 (4.70%)	1.81 (3.01%)
(c)	0.22 (0.36%)	2.65 (4.42%)	1.89 (3.15%)	0.74 (1.23%)	1.08 (1.81%)	1.51 (2.51%)	1.35 (2.25%)

At some positions, the actuators had difficulty maintaining the commanded position and instead oscillated around the commanded position. This can be best seen in actuator

(a) of Figure 9. This may be caused in part to inherent mechanical hysteresis and the jagged force response (local mountains and valleys), shown in Figure 5, and relatively large pumps that were used in the control. Actuator (a), in particular, had a small air leak that acted as a disturbance, causing it to slowly retract when the pumps were stopped. As can be seen, the resistance measurement allowed the control system to identify and correct the effect of this disturbance.

For some of the feedback testing, control resulted in a steady-state error of a few centimeters (Figure 9). In these cases, it is clear that the controller believed the actuator was at the correct length (convergence of the dotted line with the thick black line) even as the ultrasonic sensor reported the error for post-processing (gap between the thin solid line and the thick solid line). This may be due in part to the best-fit calibration curve not fully capturing the resistance response.

8. Conclusions

The SPIRA Coil actuator presented in this work has many unique features compared to other actuators, including long extension lengths, ease of fabrication, low actuation pressure, and self-sensing. The coiled structure of the actuator allows it to extend to dramatically long lengths from a relatively small initial diameter. The actuator can be fabricated with low-cost, readily available materials and tools. The material for each actuator costs only a few US dollars. The fabrication requires little more than cutting tools and an oven. Compared to elastomer-based actuators, which often require large pressures to strain the material (e.g., 345 kPa for one of the most widely-cited soft actuators [41]), some of the SPIRA Coil prototypes tested in this work were able to self-extend with pressures lower than 5 kPa (less than 0.75 psig).

The simple spring and pneumatic models presented and validated in this work successfully approximated the experimental values. These simple-to-use algebraic models will enable SPIRA Coils to be readily designed for use in a variety of robotic applications, without the need to resort to complex and expensive computational modeling techniques.

Furthermore, the SPIRA Coils can measure their own extension through the resistance of the circuit formed by the metalized sheets, creating the opportunity for feedback control. Feedback control was successfully demonstrated on three actuators with an average measurement error of 1.2 cm (2.1%).

Compared to other potential electrical values (e.g., inductance, capacitance) resistance is by far the simplest to measure. Many implementations of resistance sensing in soft robotics, however, exhibit extreme time dependence and hysteresis due to the interaction of the resistive elements with elastomeric structures and the associated stress–relaxation [12]. In contrast, the resistance of SPIRA coils shows virtually no hysteresis (Figure 7). Though the resistance depends on the contact of two conductive surfaces, these surfaces are inside the sealed internal volume and thus are inherently protected from outside dust and debris which could foul that connection. Future work on SPIRA Coil self-sensing could include methods for preventing localized buckling along creases, preventing electrical connection along the edges, and an investigation into the effect of temperature on the resistance.

Compared to other soft actuators, SPIRA Coils can extend to dramatic lengths. They are low-cost, easy-to-fabricate, and easy-to-use. Their motion can be driven with low-pressure micro-pumps and their length can be measured through resistance. The techniques and results presented in this work represent the beginning of the investigation into SPIRA Coils. We welcome additional work to improve and extend these methods. We are confident that the robotics community will find many interesting and useful applications for this unique actuator technology.

9. Patents

Felt, Wyatt and Greenwood, Jacob R. U.S. Provisional Appl. #63/489,962. *Self-Sensing Pressure-Driven Extending Actuator*. Filed: 13 March 2023.

Supplementary Materials: The following supporting information is available: Video S1: Video abstract and SPIRA Coil feedback control demonstration, <https://youtu.be/fdyJlAw4ao>; Video S2: How to fabricate SPIRA Coils, <https://youtu.be/dUjNiWvFAJc>; Video S3: Force testing of SPIRA Coils, <https://youtu.be/Ylq9VbeD4I8>.

Author Contributions: Conceptualization, W.F. and J.R.G.; methodology, W.F. and J.R.G.; software, J.R.G. and W.F.; validation, J.R.G. and W.F.; formal analysis, W.F.; investigation, J.R.G. and W.F.; resources, W.F.; data curation, W.F.; writing—original draft preparation, W.F. and J.R.G.; writing—review and editing, W.F.; visualization, J.R.G. and W.F.; supervision, W.F.; project administration, W.F.; funding acquisition, W.F. All authors have read and agreed to the published version of the manuscript.

Funding: This material is based upon work supported by the U.S. Department of Energy, Office of Science, Office of Energy Efficiency and Renewable Energy, Building Technologies Office, under Award Number DE-SC0022837. This report was prepared as an account of work sponsored by an agency of the United States Government. Neither the United States Government nor any agency thereof, nor any of their employees, makes any warranty, express or implied, or assumes any legal liability or responsibility for the accuracy, completeness, or usefulness of any information, apparatus, product, or process disclosed, or represents that its use would not infringe privately owned rights. Reference herein to any specific commercial product, process, or service by trade name, trademark, manufacturer, or otherwise does not necessarily constitute or imply its endorsement, recommendation, or favoring by the United States Government or any agency thereof. The views and opinions of authors expressed herein do not necessarily state or reflect those of the United States Government or any agency thereof.

Data Availability Statement: The data presented in this study are available on request from the corresponding author.

Acknowledgments: The authors gratefully acknowledge the feedback and support of their colleagues at VPI Technology, especially Eric Brooksby. The authors would also like to thank the University of Utah Materials Characterization Lab for the use of their tensile test machine. This paper adapts and expands material that was presented at the 2023 ASME International Design Engineering Technical Conferences and Mechanics and Robotics Conference (IDETC/MR 2023) under the title “SPIRA Coils: Soft Self-Sensing Pneumatic Integrated Retractable Actuator Coils” [42]. The authors of the original conference paper match those of the present paper, Jacob R. Greenwood and Wyatt Felt. Copyright for that work is held by ASME and it is used here by permission.

Conflicts of Interest: The authors declare no conflict of interest. The funding sponsors had no role in the design of the study; in the collection, analyses, or interpretation of data; in the writing of the manuscript, or in the decision to publish the results.

Abbreviations

The following abbreviations and nomenclature are used in this manuscript:

ASME	American Society of Mechanical Engineers
SPIRA Coil	Soft Self-Sensing Pneumatic Integrated Retractable Actuator Coil
A_{pneu}	cross-sectional area of the inflated pneumatic chamber
b	width of a constant force spring
b_p	width of the flattened pneumatic chamber
b_t	total actuator width
D	natural diameter of the actuator at length x
D_i	inner diameter of the actuator
D_n	natural diameter of a constant force spring
D_o	outer diameter of the actuator
E	Young’s modulus
E_l	Young’s modulus of laminate-only section
E_p	Young’s modulus of pneumatic chamber
F_M	force measured by the tensile test machine
F_R	retraction force
F_E	extension force
l	total actuator length

P	pressure in pneumatic chamber
ρ_{al}	resistivity of aluminum, 2.65×10^{-8} ohm m
ΔR	resistance of the actuator
t	thickness of a constant force spring
t_{al}	thickness of aluminum on the metalized PET
t_l	thickness of laminate section
t_p	thickness of the flattened pneumatic chamber
t_s	thickness of shim material
V	volume of air in pneumatic chamber
x	deployed actuator length

References

- Xavier, M.S.; Tawk, C.D.; Zolfagharian, A.; Pinskiier, J.; Howard, D.; Young, T.; Lai, J.; Harrison, S.M.; Yong, Y.K.; Bodaghi, M.; et al. Soft pneumatic actuators: A review of design, fabrication, modeling, sensing, control and applications. *IEEE Access* **2022**, *10*, 59442–59485. [\[CrossRef\]](#)
- Pagoli, A.; Chapelle, F.; Corrales-Ramon, J.A.; Mezouar, Y.; Lapusta, Y. Review of soft fluidic actuators: Classification and materials modeling analysis. *Smart Mater. Struct.* **2021**, *31*, 013001. [\[CrossRef\]](#)
- El-Atab, N.; Mishra, R.B.; Al-Modaf, F.; Joharji, L.; Alsharif, A.A.; Alamoudi, H.; Diaz, M.; Qaiser, N.; Hussain, M.M. Soft actuators for soft robotic applications: A review. *Adv. Intell. Syst.* **2020**, *2*, 2000128. [\[CrossRef\]](#)
- Veale, A.J.; Xie, S.Q.; Anderson, I.A. Characterizing the Peano fluidic muscle and the effects of its geometry properties on its behavior. *Smart Mater. Struct.* **2016**, *25*, 065013. [\[CrossRef\]](#)
- Daerden, F.; Lefeber, D. The concept and design of pleated pneumatic artificial muscles. *Int. J. Fluid Power* **2001**, *2*, 41–50. [\[CrossRef\]](#)
- Joe, S.; Bernabei, F.; Beccai, L. A Review on Vacuum-Powered Fluidic Actuators in Soft Robotics. In *Rehabilitation of the Human Bone-Muscle System*; IntechOpen: London, UK, 2022.
- Felt, W.; Robertson, M.A.; Paik, J. Modeling vacuum bellows soft pneumatic actuators with optimal mechanical performance. In Proceedings of the 2018 IEEE International Conference on Soft Robotics (RoboSoft), Livorno, Italy, 24–28 April 2018; IEEE: Piscataway, NJ, USA, 2018; pp. 534–540.
- Li, S.; Vogt, D.M.; Rus, D.; Wood, R.J. Fluid-driven origami-inspired artificial muscles. *Proc. Natl. Acad. Sci. USA* **2017**, *114*, 13132–13137. [\[CrossRef\]](#) [\[PubMed\]](#)
- Hawkes, E.W.; Blumenschein, L.H.; Greer, J.D.; Okamura, A.M. A soft robot that navigates its environment through growth. *Sci. Robot.* **2017**, *2*, eaan3028. [\[CrossRef\]](#)
- Felt, W. An Inverting-Tube Clutching Contractile Soft Pneumatic Actuator. *arXiv* **2019**, arXiv:1903.02725.
- Hammond, Z.M.; Usevitch, N.S.; Hawkes, E.W.; Follmer, S. Pneumatic reel actuator: Design, modeling, and implementation. In Proceedings of the 2017 IEEE International Conference on Robotics and Automation (ICRA), Singapore, 29 May–3 June 2017; IEEE: Piscataway, NJ, USA, 2017; pp. 626–633.
- Felt, W. Sensing Methods for Soft Robotics. Ph.D. Thesis, University of Michigan, Ann Arbor, MI, USA, 2017.
- Nomura, K.; Takeuchi, H.; Sato, M.; Ishii, H.; Uemura, M.; Akaboshi, T.; Tomikawa, M.; Hashizume, M.; Takanishi, A. Development of a Self-Propelled Actively Bendable Colonoscope Robot with a “Party Horn” Propulsion Mechanism. In Proceedings of the Abstracts of the International Conference on Advanced Mechatronics: Toward Evolutionary Fusion of IT and Mechatronics: ICAM 2015.6, Tokyo, Japan, 5–8 December 2015; The Japan Society of Mechanical Engineers: Tokyo, Japan, 2015; pp. 68–69.
- Schenk, M.; Viquerat, A.D.; Seffen, K.A.; Guest, S.D. Review of inflatable booms for deployable space structures: Packing and rigidization. *J. Spacecr. Rocket.* **2014**, *51*, 762–778. [\[CrossRef\]](#)
- Secheli, G.A. *Modelling of Packaging Folds in Metal-Polymer Laminates*; University of Surrey: Guildford, UK, 2018.
- Fernandez, J.M. Low-Cost Gossamer Systems for Solar Sailing and Spacecraft Deorbiting Applications. Ph.D. Thesis, University of Surrey, Guildford, UK, 2014.
- Grande, A.M. Preliminary Analysis of Innovative Inflatable Habitats for Mars Surface Missions. Master’s Thesis, Politecnico di Milano, Milan, Italy, 2020.
- Secheli, G.; Viquerat, A.; Aglietti, G.S. A model of packaging folds in thin metal-polymer laminates. *J. Appl. Mech.* **2017**, *84*, 101005. [\[CrossRef\]](#)
- Kamaliya, P.K.; Upadhyay, S.H.; Mallikarachchi, H. Investigation of wrinkling behaviour in the creased thin-film laminates. *Int. J. Mech. Mater. Des.* **2021**, *17*, 899–913. [\[CrossRef\]](#)
- Katsumata, N.; Fujii, R.; Natori, M.; Yamakawa, H. Models of Membrane Space Structures with Inflatable Tubes. *Trans. Jpn. Soc. Aeronaut. Space Sci. Aerosp. Technol. Jpn.* **2010**, *8*, Pc_59–Pc_65. [\[CrossRef\]](#) [\[PubMed\]](#)
- Arya, M.; Lee, N.; Pellegrino, S. Crease-free biaxial packaging of thick membranes with slipping folds. *Int. J. Solids Struct.* **2017**, *108*, 24–39. [\[CrossRef\]](#)
- Zirbel, S.A.; Lang, R.J.; Thomson, M.W.; Sigel, D.A.; Walkemeyer, P.E.; Trease, B.P.; Magleby, S.P.; Howell, L.L. Accommodating thickness in origami-based deployable arrays. *J. Mech. Des.* **2013**, *135*, 111005. [\[CrossRef\]](#)

23. Bolanos, D.; Varela, K.; Sargent, B.; Stephen, M.A.; Howell, L.L.; Magleby, S.P. Selecting and Optimizing Origami Flasher Pattern Configurations for Finite-Thickness Deployable Space Arrays. *J. Mech. Des.* **2023**, *145*, 023301. [[CrossRef](#)]
24. Fang, H.; Lou, M.; Hah, J. Deployment study of a self-rigidizable inflatable boom. *J. Spacecr. Rocket.* **2006**, *43*, 25–30. [[CrossRef](#)]
25. Wang, J.T. *Deployment Simulation Methods for Ultra-Lightweight Inflatable Structures*; National Aeronautics and Space Administration, Langley Research Center: Hampton, VA, USA, 2003.
26. Yuan, T.; Tang, L.; Liu, J. Dynamic modeling and analysis for inflatable mechanisms considering adhesion and rolling frictional contact. *Mech. Mach. Theory* **2023**, *184*, 105295. [[CrossRef](#)]
27. Fay, J.; Steele, C. Forces for rolling and asymmetric pinching of pressurized cylindrical tubes. *J. Spacecr. Rocket.* **1999**, *36*, 531–537. [[CrossRef](#)]
28. Steele, C.; Fay, J. Inflation of rolled tubes. In Proceedings of the IUTAM-IASS Symposium on Deployable Structures: Theory and Applications: Proceedings of the IUTAM Symposium, Cambridge, UK, 6–9 September 1998; Springer: Dordrecht, The Netherlands, 2000; pp. 393–403.
29. Sandy, C.; Cadogen, D. Inflatable structures for space applications. *Nasa Tech. Memo.* **2000**, 208577, 90–97.
30. Chen, T.; Wen, H.; Jin, D.; Hu, H. New design and dynamic analysis for deploying rolled booms with thin wall. *J. Spacecr. Rocket.* **2016**, *53*, 225–230. [[CrossRef](#)]
31. Schenk, M.; Kerr, S.; Smyth, A.; Guest, S. Inflatable cylinders for deployable space structures. In Proceedings of the First Conference Transformables, Seville, Spain, 18–20 September 2013; Volume 9, pp. 1–6.
32. Viquerat, A.; Schenk, M.; Lappas, V.; Sanders, B. Functional and qualification testing of the InflateSail technology demonstrator. In Proceedings of the 2nd AIAA Spacecraft Structures Conference, Kissimmee, FL, USA, 5–9 January 2015; p. 1627.
33. Taber, R.E. Method of Making a Self-Coiling Sheet, US Patent 3,426,115, 4 February 1969.
34. Sargent, B.; Brown, N.; Jensen, B.D.; Magleby, S.P.; Pitt, W.G.; Howell, L.L. Heat set creases in polyethylene terephthalate (PET) sheets to enable origami-based applications. *Smart Mater. Struct.* **2019**, *28*, 115047. [[CrossRef](#)]
35. Sargent, B.; Butler, J.; Seymour, K.; Bailey, D.; Jensen, B.; Magleby, S.; Howell, L. An origami-based medical support system to mitigate flexible shaft buckling. *J. Mech. Robot.* **2020**, *12*, 041005. [[CrossRef](#)]
36. Klett, Y. Paleo: Plastically annealed lamina emergent origami. In Proceedings of the International Design Engineering Technical Conferences and Computers and Information in Engineering Conference, Quebec City, QC, Canada, 26–29 August 2018; American Society of Mechanical Engineers: New York, NY, USA, 2018; Volume 51814, p. V05BT07A062.
37. Hyatt, L.P.; Lytle, A.; Magleby, S.P.; Howell, L.L. Designing Developable Mechanisms From Flat Patterns. In Proceedings of the International Design Engineering Technical Conferences and Computers and Information in Engineering Conference, Online, 17–19 August 2020; American Society of Mechanical Engineers: New York, NY, USA, 2020; Volume 83990, p. V010T10A013.
38. Greenwood, J.; Avila, A.; Howell, L.; Magleby, S. Conceptualizing stable states in origami-based devices using an energy visualization approach. *J. Mech. Des.* **2020**, *142*, 093302. [[CrossRef](#)]
39. Votta, F., Jr. The theory and design of long-deflection constant-force spring elements. *Trans. Am. Soc. Mech. Eng.* **1952**, *74*, 439–447. [[CrossRef](#)]
40. Peressini, A.L. Comparing Solutions of the Paper Roll Problem. In Proceedings of the Metropolitan Mathematics Club of Chicago, Chicago, IL, USA, 6 February 2009. Available online: http://mtl.math.uiuc.edu/special_presentations/JoansPaperRollProblem.pdf (accessed on 28 October 2023).
41. Mosadegh, B.; Polygerinos, P.; Keplinger, C.; Wennstedt, S.; Shepherd, R.F.; Gupta, U.; Shim, J.; Bertoldi, K.; Walsh, C.J.; Whitesides, G.M. Pneumatic networks for soft robotics that actuate rapidly. *Adv. Funct. Mater.* **2014**, *24*, 2163–2170. [[CrossRef](#)]
42. Greenwood, J.R.; Felt, W. SPIRA Coils: Soft Self-Sensing Pneumatic Integrated Retractable Actuator Coils. In Proceedings of the 47th Mechanisms and Robotics Conference (MR), International Design Engineering Technical Conferences and Computers and Information in Engineering Conference, Boston, MA, USA, 20–23 August 2023; Volume 8.

Disclaimer/Publisher’s Note: The statements, opinions and data contained in all publications are solely those of the individual author(s) and contributor(s) and not of MDPI and/or the editor(s). MDPI and/or the editor(s) disclaim responsibility for any injury to people or property resulting from any ideas, methods, instructions or products referred to in the content.